Free-electron effects on the optical absorption of the hybrid perovskite CH$_3$NH$_3$PbI$_3$ from first principles

Joshua Leveillee[1] and André Schleife[1,2,3,*]

[1]*Department of Materials Science and Engineering, University of Illinois at Urbana-Champaign, Urbana, Illinois 61801, USA*
[2]*Materials Research Laboratory, University of Illinois at Urbana-Champaign, Urbana, Illinois 61801, USA*
[3]*National Center for Supercomputing Applications, University of Illinois at Urbana-Champaign, Urbana, Illinois 61801, USA*

Hybrid organic-inorganic perovskites, such as methylammonium lead tri-iodide (MAPbI$_3$), are interesting candidates for efficient absorber materials in next-generation solar cells, partly due to an unusual combination of low exciton-binding energy and strong optical absorption. Excitonic effects in this material have been subject to debate both for experiment and theory, indicating a need for better understanding of the screening mechanisms that act upon the electron-hole interaction. Here, we use cutting-edge first-principles theoretical spectroscopy, based on density-functional and many-body perturbation theory, to study atomic geometries, electronic structure, and optical properties of three MAPbI$_3$ polymorphs and find good agreement with earlier results and experiment. We then study the influence of free electrons on the electron-hole interaction and show that this explains consistently smaller exciton-binding energies, compared to those in the material without free electrons. Interestingly, we also find that the absorption line shape strongly resembles that of the spectrum without free electrons up to high free-electron concentrations. We explain this unexpected behavior by formation of Mahan excitons that dominate the absorption edge, making MAPbI$_3$ robust against free-electron-induced changes observed in other semiconductors.

I. INTRODUCTION

Hybrid organic-inorganic perovskites have seen unprecedented development over the past years, largely motivated by their potential as highly efficient absorber materials for next-generation solar cells. Research on these materials for optoelectronic applications originates as far back as the 1990s; hybrid perovskites were initially reported as dye sensitizers in TiO$_2$ scaffolds in 2006 [1,2]. Since their development as thin-film mesosuperstructured photovoltaics in 2012 [3], their photoconversion efficiency has risen to over 22.7% [4–7]. The most commonly studied material in this context is methylammonium (MA) lead tri-iodide (MAPbI$_3$) with MA = CH$_3$NH$_3$, owing to cheap solution synthesis and high-performance metrics. Besides photovoltaic applications, MAPbI$_3$ and its stoichiometric counterparts MA(Pb, Sn)(I, Br, Cl)$_3$ have shown promise in quantum dot fluorescence [8], light-emitting diodes [9], and catalysis for water splitting [10]. Along with experimental development of advanced optoelectronic technologies, extensive first-principles investigations have been undertaken to better understand the structure and band-gap trends in hybrid perovskite solar cell materials [11–16].

In addition to interesting applications, the combination of organic and heavy-metal constituents renders MAPbI$_3$ an ideal candidate to study fundamental phenomena. One example is the strong spin-orbit interaction due to heavy atoms, that heavily reduces the band gap and dominates band dispersion near the conduction-band minimum [16–18]. Another example, critically influencing whether a material is a good candidate for a photovoltaic absorber, is the electron-hole interaction: If it is strong in a material, strongly bound excitonic states appear near the absorption onset. These are associated with strong optical absorption that is beneficial for harvesting light using as little absorber material as possible. At the same time, strong electron-hole interaction renders separation of electron-hole pairs challenging, which is detrimental in a photovoltaic device [19]. Interestingly, MAPbI$_3$ balances between low exciton-binding energy and large optical absorption across the visible spectrum. This facilitates efficient generation of electron-hole pairs that can be thermally separated and is beneficial for photocurrent generation [20].

This interesting balance triggered numerous studies, aimed at a better understanding of excitonic effects in MAPbI$_3$. Experimental results for exciton-binding energies range from as high as 62 meV to as low as 2 meV [20], however, a few patterns emerge. First, the line shape of the absorption edge has been reported to be comparable to that of GaAs with no clear excitonic peak and a binding energy potentially under 10 meV at room temperature (RT) [21]. Second, a reduction of the exciton-binding energy is observed when going from the low-temperature (LT) orthorhombic phase to the RT tetragonal phase. Sestu *et al.* measured 34 meV (LT) to 29 meV (RT) [22], Galkowski *et al.* measured between 14 and 25 meV (LT) to 12 meV (RT) [23], and Yang *et al.* measured 16 meV (LT) to between 5 and 12 meV (RT) [24]. However, there are also examples for studies where RT exciton-binding energies exceed LT-binding energies in others [22–30].

*schleife@illinois.edu

Further insight into this variability comes from four-wave mixing spectroscopy to disentangle exciton-binding energies of intrinsic and defect-bound excitons [31]. These results indicate that intrinsic excitons have an LT-binding energy of 13 meV, whereas values for defect-bound excitons average around 29 meV, linking the variability to different defect concentrations lest uncharacterized. In particular, although exciton-binding energies in pure MAPbI$_3$ are consistently lower than 35 meV for LT and RT phases, the addition of small amounts of chlorine into MAPbI$_3$ thin films tends to increase this value to more than 50 meV [25,32].

Although the variation of experimental results causes ongoing debate of the excitonic character of the absorption edge, first-principles theoretical spectroscopy can provide deeper understanding. To this end, Bokdam *et al.* used many-body perturbation theory (MBPT) and solved the Bethe-Salpeter equation (BSE) for the optical polarization function, reporting an exciton-binding energy of 45 meV in tetragonal MAPbI$_3$ [33]. Similarly, Zu *et al.* computed 40 meV [34] and Umari *et al.* computed 30 meV using a similar framework [35]. All three studies attribute the dielectric screening of the electron-hole Coulomb interaction exclusively to electronic interband transitions, corresponding to a high-frequency dielectric constant ε_∞ of MAPbI$_3$ between 5 and 7 [33–35]. In another work, Ahmed *et al.* [36] used the BSE framework to predict a binding energy of 153 meV. Although these calculations were performed on a coarse $4 \times 4 \times 4$ **k**-point grid, likely leading to an overestimate of the binding energy [36], the values of 45 meV [33] and 40 meV [34] quoted above still overestimate experimental data.

However, exciton-binding energies are critically influenced by the strength of the electron-hole interaction and, thus, dielectric screening in the material, both in experiment and in calculations. This is important because the lattice structure of MAPbI$_3$ is very polarizable, leading to a large *static* dielectric constant, possibly contributing to screening. To this end, Frost *et al.* showed that the static dielectric constant of 25.7, accounting for lattice and electronic polarizability, leads to an exciton-binding energy of less than 1 meV in a Wannier-Mott model [37]. Evens *et al.* used a value of $\varepsilon = 11$ to demonstrate that including lattice contributions to screening improves agreement with measured room-temperature absorption spectra [38]. Menéndez-Proupin *et al.* use a parabolic band with a Pollman-Büttner-type model for polaron screening and find an exciton binding energy of 24 meV [39]. Umari *et al.* also showed that including polar phonon screening reduces the binding energy from 30 to 15 meV [35]. Finally, Hakamata *et al.* employed nonadiabatic molecular dynamics (MD) to calculate the time-averaged exciton-binding energy in a dynamical MAPbI$_3$ lattice, predicting a binding energy of 12 meV and a dielectric constant between 10 and 15, in excellent agreement with RT measured values [40]. Bokdam *et al.* provide arguments against the importance of lattice screening for exciton-binding energies of MAPbI$_3$ and instead invoke formation of polarons [33].

In this paper, we study the complementary problem of an additional screening contribution due to free electrons, arising from defects or donors in a sample. First-principles studies of multiple point defects in MAPbI$_3$ showed that charged defects with low formation energy occupy shallow levels relative to

the band extrema [41–44]. Wang *et al.* showed that synthesis with varying ratios of PbI$_2$:MAI precursors can change samples from *p* to *n* type with free-electron concentrations as high as 3.5×10^{18} cm^{-3} and even at a standard precursor ratio of 1:1 moles of PbI$_2$ and MAI, a free-electron concentration of 1.8×10^{17} cm^{-3} was measured [45]. Other studies confirmed free-carrier concentrations in the range of 10^{17}–10^{18} cm^{-3} [46,47]. Dielectric screening due to free electrons has been shown to reduce the strength of the electron-hole Coulomb interaction in ZnO [48–50] and, together with Pauli blocking lead to the formation of Mahan excitons [51] at the absorption edge.

We speculate that these effects also affect exciton binding in MAPbI$_3$ and to clarify this, we perform accurate first-principles simulations of the electronic structure and optical properties of MAPbI$_3$. The remainder of the paper is organized as follows. Section II summarizes the theoretical and computational approach for solving the BSE to calculate the optical response. Section III details results for atomic geometries, electronic structure, and optical properties. We compute exciton-binding energies and optical spectra, explicitly including various concentrations of free electrons that arise in the material for varying defect concentrations. Finally, Sec. IV summarizes and concludes this paper.

II. COMPUTATIONAL APPROACH

We use density-functional theory (DFT) [52,53] to compute fully relaxed atomic geometries of the three experimentally most relevant polymorphs of MAPbI$_3$, i.e., the orthorhombic (*O*), tetragonal (*T*), and cubic (*C*) phases. Their Brillouin zones (BZs) are sampled using Γ-centered $4 \times 4 \times 4$, $4 \times 4 \times 4$, and $6 \times 6 \times 6$ **k**-point meshes, respectively. The projector-augmented wave (PAW) method is used to describe the electron-ion interaction [54] and single-particle wave functions are expanded into a plane-wave basis up to a cutoff energy of 600 eV. These parameters are sufficient to converge the total energy to within 5 meV per atom. The Perdew-Burke-Ernzerhof for solids (PBEsol) exchange-correlation (XC) functional [55] has previously been used to predict accurate relaxed atomic geometries for MAPbI$_3$ [56] and is used here for the same purpose.

In order to obtain equilibrium atomic geometries, we initialize the structures of the *O*, *T*, and C phases prior to relaxation using those reported in Ref. [56]. This captures the symmetry of ordered MA cations in the *O* phase and a pseudorandom ordering of the MA sublattice in the *T* phase. Although the *C* phase exhibits total disordering of the MA cation sublattice in experiment [57], we study a pseudocubic phase with ordered MA cations. This approach is common in the literature to maintain the uniform alignment of PbI$_3$ octahedra observed experimentally for the *C* phase [56,58,59]. In experiment, the cubic lattice also shows a slight pseudocubic behavior due to rotations of the MA cations [57]. We verify that these atomic coordinates correspond to equilibrium structures by computing total energies for several unit-cell volumina within 1% of the equilibrium value and determine the minimum. All atomic geometries were then relaxed until Hellman-Feynman forces were smaller than 10 meV/Å.

For these relaxed geometries, we compute high- and low-frequency dielectric tensors using density-functional perturbation theory (DFPT) [60] and the PBE generalized-gradient approximation [61] to describe XC. The BZs are sampled using Γ-centered $5 \times 5 \times 5$, $5 \times 5 \times 5$, and $7 \times 7 \times 7$ **k**-point meshes for O, T, and C phases, respectively, for these calculations.

In order to compute electronic structures that can be compared to experiment, we overcome the well-known band-gap underestimation of DFT by taking quasiparticle (QP) corrections into account within MBPT [62]. Furthermore, due to the presence of heavy-metal ions in MAPbI$_3$, spin-orbit coupling (SOC) is included within the PAW approach [63]. We performed GW$_0$ + SOC calculations using $1 \times 1 \times 1$, $1 \times 1 \times 1$, and $2 \times 2 \times 2$ Γ-centered **k**-point grids for O, T, and C phases, respectively. The Green's function was iterated four times to converge QP band gaps to within 25 meV. Four thousand empty bands were included for the O and T structures and 2000 for the C phase.

Finally, we study optical response including excitonic effects by solving the BSE for the optical polarization function. The BSE in the Bloch basis can be written as an eigenvalue equation [64,65] for the Hamiltonian,

$$H(cv\mathbf{k}, c'v'\mathbf{k}') = (\epsilon_{c\mathbf{k}} - \epsilon_{v\mathbf{k}})\delta_{cc'}\delta_{vv'}\delta_{\mathbf{kk}'} + 2v_{c'v'\mathbf{k}'}^{cv\mathbf{k}} - W_{c'v'\mathbf{k}'}^{cv\mathbf{k}}. \tag{1}$$

The indices c, v, and **k**, refer to the conduction band, the valence band, and the point in reciprocal space, respectively. The term in parentheses on the right-hand side represents single-QP excitation energies of noninteracting electron-hole pairs, described by the QP band structure. For the QP energies $\epsilon_{c\mathbf{k}}$ and $\epsilon_{v\mathbf{k}}$, we use results computed using PBE + SOC, with the band gap rigidly shifted to the GW$_0$ + SOC gap. Bloch integrals, that enter the exchange interaction $2v_{c'v'\mathbf{k}'}^{cv\mathbf{k}}$ and the screened Coulomb interaction $W_{c'v'\mathbf{k}'}^{cv\mathbf{k}}$ between electrons and holes, are evaluated using spin-polarized DFT-PBE Kohn-Sham eigenstates. Electronic interband screening of the electron-hole Coulomb interaction is computed using the model dielectric function proposed by Bechstedt *et al.* [66] and Capellini [67] in the absence of free carriers [66,67] and approximated as a dielectric constant ε_∞ when free carriers are taken into account [48,49]. Optical spectra of C MAPbI$_3$ are computed over a wide energy range using a $11 \times 11 \times 11$ **k**-point grid with a small random shift and for a careful examination of the spectral onset up to an energy of 2.2 eV, a hybrid 5:2:32.5 **k**-point grid is used (see Ref. [65] for nomenclature). Independent-particle spectra for the O and T phases were computed using $7 \times 7 \times 7$ **k** points with a small random shift.

In order to describe the influence of free electrons, we account for: (i) Pauli blocking affecting selection rules for optical transitions [Burstein-Moss shift (BMS)], (ii) free-electron effects on the single-particle band structure via band-gap renormalization (BGR), and (iii) additional free-electron screening of the electron-hole interaction [48,50,68,69]. This approach has been previously successfully used to describe optical properties of doped ZnO [48,49]. BMS arises from Pauli blocking of the lowest conduction-band states that are occupied by the additional free electrons. We account for this

by setting the occupation number of these states accordingly when calculating dielectric functions after the ground-state DFT electronic-structure calculations. BGR is described as a rigid shift of the entire conduction band, computed using the analytic model of Berggren and Sernelius [70], presented in the Supplemental Material [71]. The model describes two contributions to the electronic self-energy: (i) the decreased electron-electron exchange energy attributed to enhanced screening by the Fermi gas of free carriers in the conduction band and (ii) the self-scattering of free carriers, referred to as impurity-impurity scattering. Finally, free-carrier screening of the electron-hole Coulomb interaction in the BSE is approximated in this paper as a free-electron-like response via an intraband Thomas-Fermi contribution to dielectric screening. This is described in detail in Refs. [48,50] and in the Supplemental Material [71] of this paper. We note that, in the literature, free-carrier screening also has been approximated using Debye screening for nondegenerate free-carrier concentrations [72].

All DFT and GW calculations are carried out using the Vienna *ab initio* simulation package [60,73–75]. The BSE calculations are performed using the implementation described in Refs. [65,76]. All input and output of this paper are available in the Materials Data Facility [77].

III. RESULTS AND DISCUSSION

A. Atomic geometries

First, we study relaxed atomic geometries of the low-temperature equilibrium phase of MAPbI$_3$, the O crystal structure with space-group $Pnma$ [57,78]. This phase has minimum entropy by ordering CH$_3$NH$_3$ ions periodically [56], and the PbI$_3$ sublattice forms stacked octahedra that are tilted with respect to the [001] axis of the unit cell (see Fig. 1). Angles between lattice vectors are all $90°$, and the lattice parameters are nonequal with $a = 8.37$, $b = 9.07$, and $c = 12.67$ Å. The c axis agrees well with experimental values between 12.1 and 12.6 Å, and the relaxed a:b aspect ratio in this paper of 0.921 only slightly underestimates that seen in experiments 0.97–0.98 [57,79]. Experiment also shows that, above $T = 162$ K, MAPbI$_3$ undergoes a phase transformation to a T phase with space-group $I4/mcm$ (see Fig. 1) [57,78]. This first-order phase transition is marked by three phenomena: First, we compute a change in lattice parameters from $a \neq b \neq c$ in the O to $a = 8.70$, $b = 8.72$, and $c = 12.83$ Å in the T phase. The relaxed structure results in good agreement between a and b with a difference of only ≈ 0.02 Å. Second, there is disordering of CH$_3$NH$_3$ ions in the T phase, that leads to a disordered cation sublattice. To approximate this effect in our unit cell, we disorder the organic cations based on the structures of Brivio *et al.* [56]. This disorder is stabilized by c-axis tilting in the T phase. Finally, alternating tilts of the octahedrons in the [001] direction appear, which, in turn, stabilizes the $a = b$ condition [57,78].

At even higher temperatures above $T = 327$ K, T MAPbI$_3$ undergoes another transition to a C phase with space-group $Pm\bar{3}m$ (see Fig. 1) [78]. This C phase is stabilized through total disordering of the MA cation sublattice. Since thermal rotation of MA cations is not accounted for in
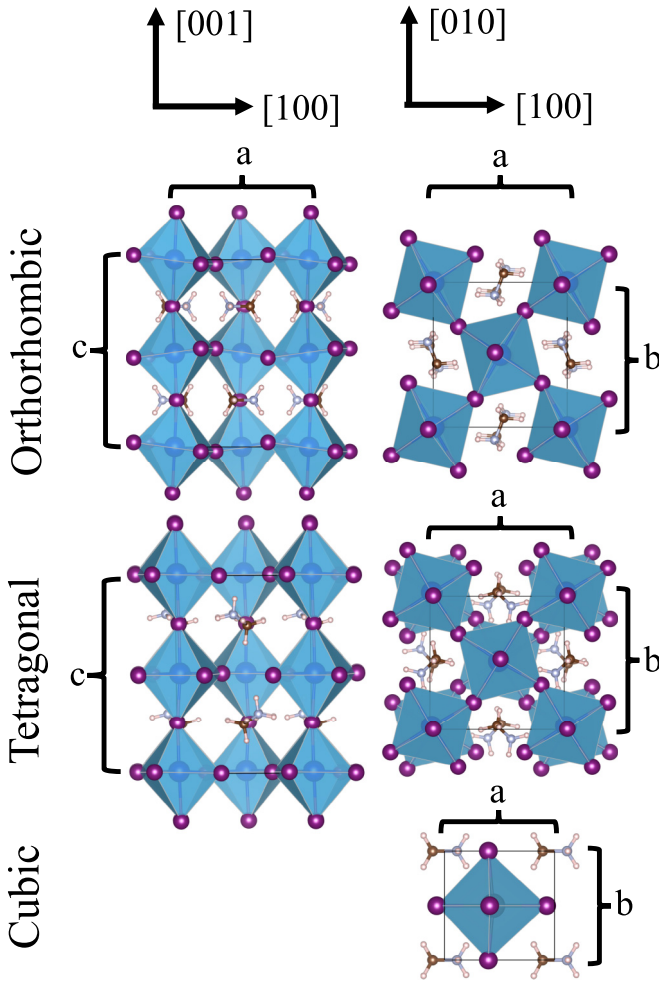
FIG. 1. Relaxed atomic geometries of orthorhombic, tetragonal, and cubic phases of MAPbI$_3$. Ions are represented as gray (Pb), purple (I), brown (C), pink (H), and blue (N) spheres. Lattice constants a, b, and c align with the [001], [010], and [001] directions, respectively.

the geometry relaxation [57], we follow the common approach of modeling this phase as a pseudocubic distortion of the $Pm\bar{3}m$ cubic perovskite structure with ordered MA cations [57,78]. This lattice geometry is slightly triclinic; in experiment, it is also pseudocubic due to rotations of the MA cations [57]. Relaxed atomic geometries result in slightly tilted axes compared to the experimental $Pm\bar{3}m$ phase, which agrees with earlier computational reports: Ong *et al.* showed that, in DFT calculations, the distorted C phase (space-group $P4mm$) is more stable compared to a constrained $Pm\bar{3}m$ phase [78]. The average of the pseudocubic lattice constants $(a + b + c)/3 = 6.31$ Å agrees well with measurements [57].

Overall, our results for relaxed atomic geometries are in excellent agreement with values from experiment and previous calculations. A more detailed comparison to other work can be found in Table S1 of the Supplemental Material [71].

B. Electronic structure

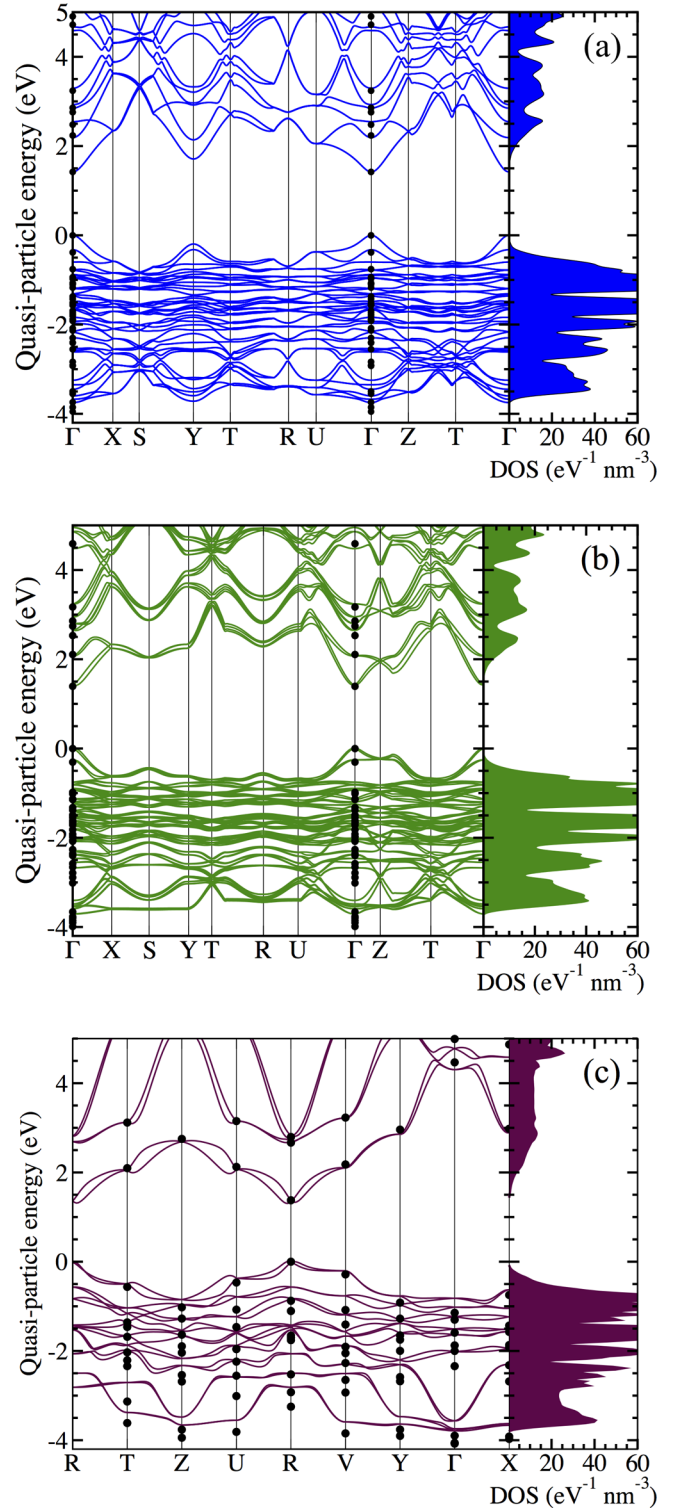Using the GW$_0$ + SOC approach, we compute band gaps of 1.42, 1.39, and 1.38 eV, for the O, T, and C phases,

FIG. 2. Kohn-Sham band structure and density of states from PBE + $\Delta_{\mathrm{GW_0}}$ + SOC (solid lines) and GW$_0$ + SOC (black circles) calculations for (a) orthorhombic, (b) tetragonal, and (c) cubic phases of MAPbI$_3$. All conduction states are rigidly shifted to the GW$_0$ + SOC gap. The valence-band maximum is used as energy zero.

respectively (see Table I). Figure 2 shows direct band gaps for each phase that are located at the Γ point of the BZ for the O and T phases and at the R point for the C phase. This change in reciprocal-space location of the direct gap is a

TABLE I. Band-gaps E_g (in eV), static (ε_0), static electronic (ε_∞) dielectric constants, and effective electron (m_c) masses for MAPbI$_3$ from our calculations and the literature. Results from G_0W_0, GW_0 (iteration only of the Green's function), $SS\text{-}GW$ (self-consistent scissor GW [80]), and quasiparticle self-consistent $GW(QSGW)$ are shown for E_g. DFPT and MD are compared for dielectric constants.

	Orthorhombic	Tetragonal	Cubic
E_g (PBE)	1.55	1.40	1.51
E_g (PBE + SOC)	0.66	0.70	0.56
E_g (GW_0 + SOC)	1.42	1.39	1.38
E_g (PBE)	1.61 [81]	1.45 [81], 1.68 [62]	1.44 [81]
E_g (G_0W_0 + SOC)	1.81 [82], 1.32 [80]	1.62 [62], 1.67 [82]	1.28 [82], 1.48 [36]
E_g ($SS\text{-}GW + SOC$)	1.79 [80,83]		
E_g ($QSGW + SOC$)			1.67 [84]
E_g (Expt.)	1.65 [82]	1.5–1.61 [82]	1.69 [82]
ε_∞ (DFPT)	6.22	6.23	6.24
ε_0 (DFPT)	23.17	22.66	22.1
ε_∞ (DFPT)	5.80 [85]	5.50 [62], 6.60 [35]	6.83 [33]
E_g (Expt.)		5.00 [86]	
ε_0 (DFPT)	25.30 [85]		
ε_0 (MD)		30.00 [33]	
E_g (Expt.)		33.50 [86], 28.80 [87]	
m_c (PBE + SOC)	0.19	0.16	0.23
m_c (DFT + SOC)	0.19 [88], 0.11 [83]	0.15 [37]	0.23 [89]
m_c (G_0W_0 + SOC)	0.16 [83]	0.17 [62]	
m_c ($SS\text{-}GW + SOC$)	0.21 [83]		

consequence of cell symmetry [90]. Our results for MAPbI$_3$ band gaps are consistent with previous GW calculations and only slightly underestimate experimental values of 1.5–1.7 eV (see Table I). This table also shows that previous calculations produced varying results based on the specific GW approximation and description of SOC [17,18,62,91]. In particular, Filip and Giustino [80] showed that different schemes for including relativistic effects and iterating the GW method resulted in different values for the gap. Using fully relativistic pseudopotentials for Pb and I and the scissor-self-consistent GW method [80] to iterate QP wave functions and eigenenergies, they predicted 1.79 eV for the orthorhombic phase [80]. Separately, Umari *et al.* reported 1.62 eV for the T phase [62].

As expected, gaps at the PBE + SOC level of theory severely underestimate experimental results by more than 1 eV for each phase. Using our GW_0 + SOC data, we can correct this for the calculation of optical spectra using a rigid scissor shift; we denote this approach by PBE + Δ_{GW_0} + SOC. Figure 2 compares band structures of O, T, and C MAPbI$_3$ at the PBE + Δ_{GW_0} + SOC and GW_0 + SOC levels of theory and illustrates the density of states (PBE + Δ_{GW_0} + SOC). In Fig. 2(c), the perfectly direct nature of the gap is broken by Rashba-Dresselhaus spin-orbit splitting for C MAPbI$_3$. However, the effect is small and hard to discern in Fig. 2(c). The effect is even smaller for T MAPbI$_3$ and has been studied extensively for T and C phases [18,92,93].

By comparing GW_0 + SOC energies at high-symmetry **k** points to the electronic structure from PBE + Δ_{GW_0} + SOC in Fig. 2, we illustrate for C MAPbI$_3$ that the latter is a suitable basis for optical calculations. Here, we are interested in the optical response in the visible spectral range, hence, we focus on electronic states within 1.6 eV of the band extrema. As can be seen in Fig. 2(c), the conduction-band dispersions from both approaches are in excellent agreement in this energy range. The Rashba-Dresselhaus split gap appears near R, and the largest deviation for the lowest conduction band amounts to about 0.15 eV at the Γ point. Overall, the valence bands are also in good agreement between both approaches. PBE + Δ_{GW_0} + SOC results tend to predict valence-band energies only slightly higher in energy than those predicted by GW_0 + SOC, for instance, 0.4 eV at the Γ point [see Fig. 2(c)]. The overall width of the uppermost valence block is 0.35 eV larger at the GW_0 + SOC level of theory. Hence, overall, our data indicate that excitation energies are underestimated by, at most, 0.3–0.4 eV when computing optical spectra starting from the PBE + Δ_{GW_0} + SOC electronic structure. Finally, effective electron masses are determined by a parabolic fit near the band edge of our PBE + Δ_{GW_0} + SOC data and reported in Table I.

C. Optical response: Independent-quasiparticle approximation

The optical absorption spectra of all three MAPbI$_3$ phases share similar spectral features as shown in Fig. 3. In this figure, we illustrate the polarization-averaged imaginary parts of the dielectric functions, computed using the independent-quasiparticle approximation within PBE + Δ_{GW_0} + SOC. Our results agree overall well in the visible region between 1.5 and 3 eV with the absorption coefficient calculated using fully relativistic GW_0 + SOC [62] for T MAPbI$_3$ as shown explicitly in Fig. S4 of the Supplemental Material [71].

Figure 3 shows a smooth gradual onset of absorption at the GW_0 band gap for all three phases. At higher energies near 2.4 eV, all spectra show a shoulder feature which we attribute to optical transitions between the uppermost valence
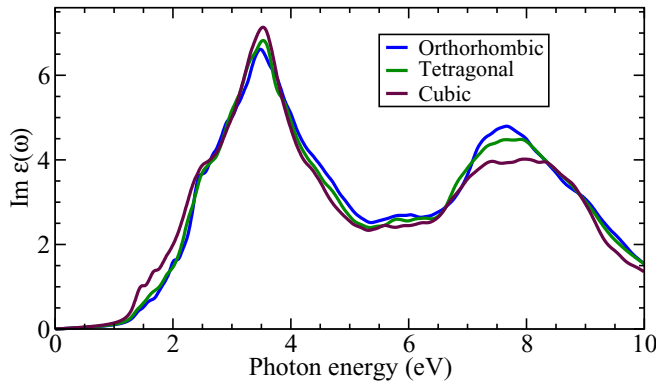
FIG. 3. Polarization-averaged imaginary part of the frequency-dependent dielectric functions of MAPbI$_3$, calculated within independent-quasiparticle approximation using PBE + Δ_{GW_0} + SOC. Blue, green, and maroon curves correspond to orthorhombic, tetragonal, and cubic phases, respectively.
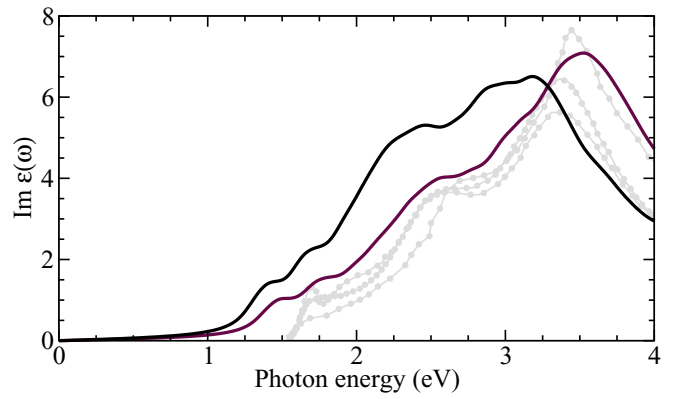

FIG. 4. Polarization-averaged imaginary part of the frequency-dependent dielectric function of cubic MAPbI$_3$. Results from independent-quasiparticle approximation, here PBE + Δ_{GW_0} + SOC (solid maroon line, identical to that in Fig. 3), are compared to the BSE$_{el}$ + Δ_{GW_0} + SOC approach (solid black line) that accounts for electron-hole interaction and to experimental [95–97] results (gray diamonds).

band and the lowest conduction band at **k** points slightly away from the location of the band extrema (see Fig. S2 in the Supplemental Material [71]). The difference in the lowest conduction and highest valence bands shows that transitions near the Γ, Y, and U points (orthorhombic), near the Γ and S points (tetragonal), and near the T, U, and V points (cubic) dominate between 2.2 and 2.6 eV. From the shoulder, ε_2 further increases into the UV energy region and peaks at 3.48, 3.53, and 3.53 eV for O, T, and C phases, respectively. The major contributions to this peak are optical transitions between the highest valence band and the lowest conduction band at **k** points far from the location of the band extrema, e.g., the Z point in C MAPbI$_3$. Figure S3 in the Supplemental Material [71] also indicates that there are minor contributions from transitions from lower valence bands into the lowest conduction band. Our assignment of these spectral features agrees with that in Ref. [20]. Finally, after this peak's optical response, ε_2 decreases until about 5.3 eV and then increases again gradually to a much broader peak, centered around 7.7 eV, which is far outside the visible spectrum.

We also computed the static (ε_0) and static electronic (ε_∞) dielectric constants of MAPbI$_3$ using DFPT and the PBE electronic structure. For ε_∞, we find very similar values around 6.23 for all three phases (see Table I). Our results are in the midst of previously calculated and measured values ranging from 5.5 to 7.0 [33,62,85,94]. We confirmed that the same magnitude but opposite sign of the quasiparticle- and SOC-induced shifts, reported before for band gaps [62], justifies using DFPT based on the PBE electronic structure to compute dielectric constants. Due to the large lattice polarizability of MAPbI$_3$, our DFPT results for ε_0 are much larger than ε_∞ with values of 22.1–23.2 for the three phases (see Table I). These results are in good agreement with earlier data from DFPT and molecular-dynamics simulations as well as experimental measurements in the range of 25–35 [86,87].

D. Optical response: Excitonic effects

Next, we study the influence of excitonic effects on optical absorption of MAPbI$_3$. To this end, Fig. 4 compares the independent-quasiparticle spectrum to the solution of the BSE, accounting for electronic interband screening as described by a model dielectric function [66,67] parametrized using a dielectric constant of $\varepsilon_\infty = 6.24$ (see Table I). Given the similarities of the independent-quasiparticle optical spectra of the three different phases (see Fig. 3), we only focus on C MAPbI$_3$ in the following.

For C MAPbI$_3$, Fig. 4 shows that excitonic effects cause a significant redshift of the absorption onset and of higher-energy features. Although the onset of the independent-quasiparticle spectrum occurs at the GW$_0$ + SOC band gap of 1.38 eV (see Table I), the lowest eigenvalue of the BSE Hamiltonian is about 64.5 meV lower in energy. Note, that this value is not a well-converged result for the exciton-binding energy due to **k**-point sampling as we discuss below [65]. Energy positions of higher-energy spectral features show larger excitonic shifts; for instance, the main peak around 3.5 eV in independent-quasiparticle approximation redshifts by about 0.5 eV. The shift is accompanied by a redistribution of spectral weight: When including excitonic effects, features at lower energies are amplified, thus, increasing the amplitude of optical absorption at lower energies.

Interestingly, in Fig. 4, positions of peaks and shoulders in the experimental spectrum seem to agree better with the independent-quasiparticle spectrum. However, we emphasize the notable difference of about 0.2–0.3 eV of the absorption onsets that is apparent in the figure and originates from the slightly smaller GW$_0$ + SOC gap, compared to experiment. If this is corrected for, e.g., by rigidly shifting the absorption onset to the experimental value, we find excellent agreement of the BSE$_{el}$ + Δ_{GW_0} + SOC result with experiment across the entire energy range, whereas the independent-particle spectrum then overestimates the position of the main peak around 3.5 eV by about 0.2–0.3 eV. In the following, we analyze how the description of the optical response changes in the presence of free electrons.
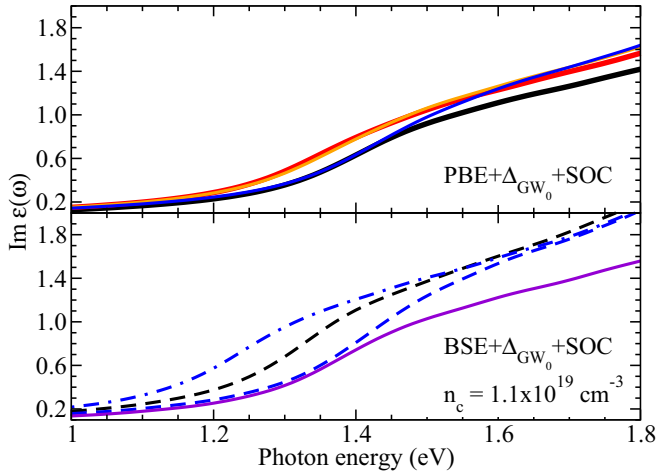
FIG. 5. Polarization-averaged imaginary part of the frequency-dependent dielectric function of C MAPbI$_3$ without free electrons (black) and with free-electron concentrations of 2.3×10^{18} cm^{-3} (red), 5.0×10^{18} cm^{-3} (orange), and 1.1×10^{19} cm^{-3} (blue). A dense hybrid 5:2:32.5 **k**-point grid was used. The top panel shows the influence of BMS and BGR on the independent-quasiparticle spectrum (PBE $+ \Delta_{GW_0} +$ SOC). The bottom panel demonstrates the influence of free electrons, $n_c = 1.1 \times 10^{19}$ cm^{-3}, on excitonic effects. The BSE$_{el} + \Delta_{GW_0} +$ SOC spectrum without free electrons (black dashed line) is compared to data that include free-electron screening without (blue dot-dashed line) and with (blue dashed line) Pauli blocking. The violet curve approximately describes lattice screening via the low-frequency dielectric constant $\varepsilon_0 = 22.1$ in the model dielectric function [67,98].

E. Optical response: Free electrons

We first study how the BMS and the BGR, i.e., two effects attributed to free electrons in the conduction band of C MAPbI$_3$, affect the independent-quasiparticle optical spectrum (see the top panel of Fig. 5). The predicted BMS due to Pauli blocking of optical transitions for a free-electron density of 10^{17} cm^{-3} is less than 2 meV and only reaches a value of about 10 meV for 10^{18} cm^{-3} (see Fig. 6). Realistic intrinsic
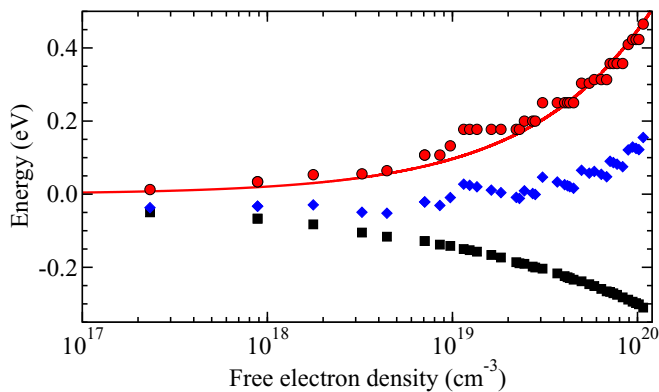

FIG. 6. Burstein-Moss shift (red circles), band-gap renormalization (black squares), and sum of both (blue diamonds) as a function of free-electron concentration in the conduction band of C MAPbI$_3$. A dense hybrid 5:2:32.5 **k**-point grid was used. The red line is a curve fit to the BMS data of the form $E_{BMS} = A n_c^{3/2}$.
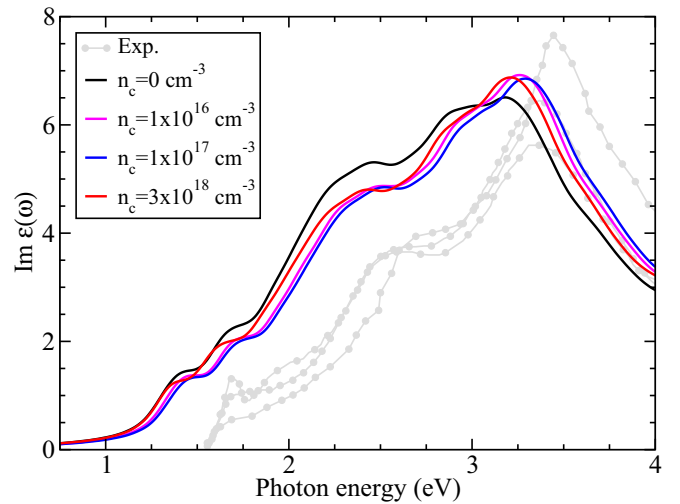

FIG. 7. Polarization-averaged imaginary part of the frequency-dependent dielectric function, computed using the BSE$_{el+fc} + \Delta_{GW_0} +$ SOC approach to account for excitonic effects. Results are shown for three different experimentally relevant free-electron concentrations and compared to data without free electrons and experiment [95–97]. As BMS and BGR are negligible for small values of n_c, they are only included for $n_c = 3 \times 10^{18}$ cm^{-3}.

n- or p-type shallow defect concentrations or free-electron-hole densities under illumination [94] fall within the range of 10^{15}–10^{17} cm^{-3}, and we conclude that for these BMSs is only a minor factor. However, we note that high-intensity illumination has produced free-carrier concentrations around 10^{19} cm^{-3} [94]. In Fig. 6, we show that, in this regime, BMS can be on the order of 0.1 eV and quickly increases thereafter, approximately following a $n_c^{3/2}$ dependence.

At the same time, Fig. 6 also illustrates that BGR is on the same order of BMS for C MAPbI$_3$ but with an opposite sign. As a result, these two effects compensate each other to very high accuracy across an unusually large free-electron range, up to about 10^{19} cm^{-3}. This explains why experimental observation of BMS $+$ BGR at the absorption edge [94,99] requires very high free-carrier concentrations: Valverde-Chávez et al. do not explicitly report [100] any effect of BMS or BGR at a free-carrier density of about 3.3×10^{17} cm^{-3}. Manser and Kamat report [94] a rise in the onset by about 0.08 eV for $n_c = 1.5 \times 10^{19}$ cm^{-3}, which is between our result for BMS and BMS $+$ BGR.

Next, in order to describe the influence of free electrons on the electron-hole interaction and, thus, excitonic effects, we describe electronic interband screening by a dielectric constant and include free-electron screening (see Eq. (S2) in the Supplemental Material [71]) when solving the BSE. Figure 7 compares the resulting imaginary part of the dielectric function of C MAPbI$_3$ without free electrons to results for three different free-electron concentrations. Although we find a blueshift of about 0.2 eV for the main absorption peak around 3 eV, interestingly, the absorption onset is almost unaffected by free electrons, both in terms of energy position and in line shape. The energy position of the absorption onset barely changes since (i) BMS and BGR largely compensate each other over a large range of free-electron concentrations

(see Fig. 6), and (ii) at the same time, the exciton binding energy is small already in the system without free electrons. Hence, its reduction in the presence of free electrons and the formation of a Mahan exciton does not lead to significant shifts of the absorption edge. Below, we discuss that this Mahan exciton is also the reason why the absorption line shape barely changes in the system with free electrons.

In addition, in Fig. 7, we compare to three experimental results [95–97]. These show good consistency for the major spectral features, i.e., the onset at 1.55 eV, the shoulder at 2.62–2.69 eV, and the peak at 3.35–3.44 eV. These peaks and shoulders are reproduced well in our simulations. The only major difference is that the computed spectra appear red-shifted with respect to experiment, which above we attributed to the difference in the single-QP band gaps (see Table I). The optical absorption bandwidth, captured by the energy difference of absorption onset and main peak, is 0.15 eV larger when free electrons are present and in slightly better agreement with experiment than the spectrum without free electrons. Also, the ratio of the dielectric function at the main peak and the shoulder at about 0.5 eV lower energies of 0.53, 0.58, and 0.66 in experiment [95–97], improves from 0.82 without free electrons to about 0.7 when accounting for free electrons. Another notable feature is the narrowing of the spectral peak width when free electrons are included, improving agreement with experiment.

Finally, in the bottom panel of Fig. 5, we illustrate the Mahan-exciton character of the line shape of the absorption spectrum near the onset for a high free-electron concentration of 1.1×10^{19} cm^{-3}. To this end, the blue curves show BSE results with (dashed) and without (dot-dashed) the effect of Pauli blocking; both include free-electron screening of the electron-hole interaction as well as BGR. Comparing these two curves, shows that Pauli blocking turns the concave line shape (dot-dashed) into a steeper more convex line shape (dashed) that resembles the case without free electrons much more closely (black dashed). Hence, this enhancement of the absorption edge can be attributed to the Fermi-edge singularity that only enters when Pauli blocking is included, which is a defining characteristic of the Mahan exciton [51]. In addition, we also compare to the result that accounts for lattice screening via the dielectric constant (violet curve) and find that, in this case, the line shape is again more concave. Thus, Fig. 5 shows that Mahan excitons are the reason that the convex line shape of the case without free electrons is largely preserved up to free-electron concentrations as large as 1.1×10^{19} cm^{-3}. Results that neglect Pauli blocking or approximately capture lattice screening lead to more concave onsets.

F. Exciton-binding energy

In order to show that the Mahan exciton, indeed, corresponds to a bound excitonic state that persists in the material despite the presence of free electrons, we computed converged exciton-binding energies as the difference between the lowest eigenvalue of the excitonic Hamiltonian and the lowest single-QP excitation energy. It has been shown before that accurate **k**-point convergence of the lowest-exciton eigenvalue is challenging and requires dense sampling of the band extrema, in particular, for Wannier-Mott-type excitons [65]. We use
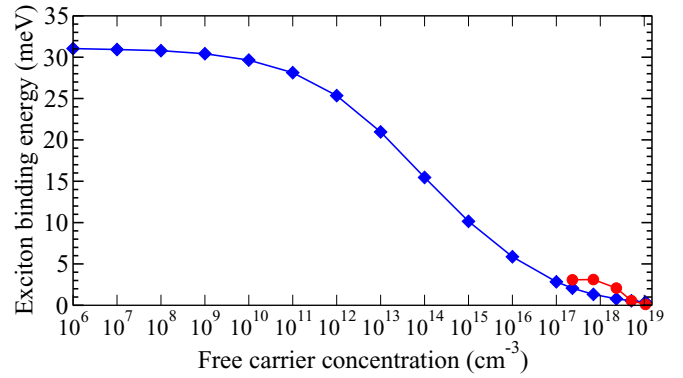

FIG. 8. Exciton-binding energy in C MAPbI$_3$ as a function of free-electron concentration, calculated using the BSE$_{el+fc}$ + Δ_{GW_0} + SOC framework. Electronic and free-electron screenings of the electron-hole interaction are included. Data with (red) and without (blue) Pauli blocking are compared.

hybrid **k**-point meshes to accomplish this and systematically increase the sampling density (see Fig. S1 in the Supplemental Material [71]). The densest grid used here samples the entire Brillouin zone by $5 \times 5 \times 5$ **k** points, but the inner third is replaced by a $14 \times 14 \times 14$ **k**-point mesh. The resulting mesh is shifted to the center around the direct gap at the R point of the BZ of C MAPbI$_3$.

The resulting value for the exciton-binding energy in C MAPbI$_3$ without free electrons is $E_b = 31.9$ meV. This is in good agreement with the highest values measured experimentally and other first-principles calculations: Umari *et al.* [35] predicted 30 meV and Bokdam *et al.* report 45 meV for the tetragonal phase [33]. The degree of Rashba-Dresselhaus shift is also higher in our paper due to a large inversion asymmetry of the relaxed pseudocubic phase, leaving fewer states closer to the band edge.

Next, we compute the change in the exciton-binding energy of C MAPbI$_3$ for finite free-electron concentrations in the conduction band using BSE calculations that account for additional free-electron screening via Eq. (S2) (see the Supplemental Material [71]). Figure 8 shows the resulting decrease in the exciton-binding energy. For free-electron concentrations around 10^{11} cm^{-3}, which is comparable to concentrations of charged and shallow defects in highly pure single-crystalline samples [101], our results show that the exciton-binding energy decreased from 31.9 to 28.13 meV. This is still above the thermal dissociation energy at room temperature and, thus, free-electron screening is not a critical factor. The data in Fig. 8 also show a significant drop in the binding energy from 25.35 to 10.15 meV for free-electron concentrations of 10^{12}–10^{15} cm^{-3}. We note that this is the range where the q_{TF}^2/q^2 term in Eq. (S2) in the Supplemental Material [71] becomes significant and, thus, free-electron screening becomes the dominant mechanism over electronic interband screening. We illustrate this explicitly in Fig. S6 of the Supplemental Material [71]. This results in the overall decline of the exciton-binding energy with increasing free-electron concentration.

At even higher free-electron concentrations between 10^{16} and 10^{17} cm^{-3}, corresponding to those observed in precursor mismatched samples [45], the exciton-binding energy is

very small, between 5.87 and 2.84 meV (see Fig. 8). Up to free-electron concentrations of $n_c \approx 2.3 \times 10^{17}$ cm^{-3}, finite **k**-point sampling prevents us from explicitly including Pauli blocking in the BSE calculations even for the most dense **k**-point grid. Hence, we explore the effect of Pauli blocking due to filling of the conduction band only for higher free-electron concentrations. For these, Fig. 8 shows an increase in the binding energy by up to 2 meV between $n = 2.3 \times 10^{17}$ and 2.3×10^{18} cm^{-3}, compared to calculations that neglect Pauli blocking. This increase has been attributed to the Fermi-edge singularity that arises when Pauli blocking is taken into account and is a characteristic feature of Mahan excitons [51]. Although the small increase in the exciton-binding energy itself is not significant enough to recover a bound exciton at room temperature in samples with a large concentration of free electrons, the Mahan exciton still dominates the line shape of the absorption edge in C MAPbI$_3$ as we discussed above for Fig. 5.

IV. CONCLUSIONS AND OUTLOOK

In this paper, we provide a thorough understanding of the absorption line shape and lowest exciton-binding energy of MAPbI$_3$. Using cutting-edge first-principles theoretical spectroscopy, based on density-functional and many-body perturbation theories, we obtain accurate results for atomic geometries, single-particle electronic structure, and two-particle optical absorption spectra. These results are a solid foundation for our analysis of free-electron-induced effects. We show that the Burstein-Moss shift and band-gap renormalization cancel each other across a large range of free-electron concentrations. By including these effects as well as free-electron-induced dielectric screening when solving the Bethe-Salpeter equation, we explain strongly reduced exciton-binding energies, compared to the material without the presence of free electrons. This elucidates how a wide range of intrinsic

free-electron concentrations in MAPbI$_3$ results in a range of exciton-binding energies between 2 and 30 meV, granting insight into a potential source of variance in experimentally measured exciton-binding energies.

Furthermore, we show that the excitons in the presence of free electrons arise from the Fermi-edge singularity, proving their Mahan-exciton character. They determine the line shape of the absorption onset and as a result, the onset still resembles that of the system without free electrons up to very high free-electron concentrations. Hence, MAPbI$_3$ largely maintains its excellent absorption properties in terms of energy position and line shape. This can explain why the material remains an excellent photovoltaic absorber even though in real samples free electrons will inevitably be present. More generally, our results make clear that additional screening of the electron-hole Coulomb interaction by free-electron effects is important in predicting accurate exciton-binding energies in MAPbI$_3$, illustrating that a deeper knowledge of electron-hole Coulomb interaction, beyond electronic interband screening, is required.

[1] M. A. Green and A. Ho-Baillie, ACS Energy Lett. **2**, 822 (2017).

[2] A. Matas Adams, J. M. Marin-Beloqui, G. Stoica, and E. Palomares, J. Mater. Chem. A **3**, 22154 (2015).

[3] M. M. Lee, J. Teuscher, T. Miyasaka, T. N. Murakami, and H. J. Snaith, Science **338**, 643 (2012).

[4] T. Ishihara, J. Lumin. **60-61**, 269 (1994).

[5] M. Saliba, T. Matsui, K. Domanski, J.-Y. Seo, A. Ummadisingu, S. M. Zakeeruddin, J.-P. Correa-Baena, W. R. Tress, A. Abate, A. Hagfeldt, and M. Grätzel, Science **354**, 206 (2016).

[6] M. Green, K. Emery, Y. Hishikawa, W. Warta, and E. Dunlop, Prog. Photovolt. Res. Appl. **24**, 905 (2016).

[7] Y. Zhou and K. Zhu, ACS Energy Lett. **1**, 64 (2016).

[8] W. Deng, H. Fang, X. Jin, X. Zhang, X. Zhang, and J. Jie, J. Mater. Chem. C **6**, 4831 (2018).

[9] L. Zhang, X. Yang, Q. Jiang, P. Wang, Z. Yin, X. Zhang, H. Tan, Y. M. Yang, M. Wei, B. R. Sutherland, E. H. Sargent, and J. You, Nat. Commun. **8**, 15640 (2017).

[10] A. R. Bin, M. Yusoff, and J. Jang, Chem. Commun. **52**, 5824 (2016).

[11] I. Borriello, G. Cantele, and D. Ninno, Phys. Rev. B **77**, 235214 (2008).

[12] F. Brivio, A. B. Walker, and A. Walsh, APL Mater. **1**, 042111 (2013).

[13] E. Mosconi, A. Amat, M. K. Nazeeruddin, M. Grätzel, and F. De Angelis, J. Phys. Chem. C **117**, 13902 (2013).

[14] Y. Wang, T. Gould, J. F. Dobson, H. Zhang, H. Yang, X. Yao, and H. Zhao, Phys. Chem. Chem. Phys. **16**, 1424 (2014).

[15] W.-J. Yin, J.-H. Yang, J. Kang, Y. Yan, and S.-H. Wei, J. Mater. Chem. A **3**, 8926 (2015).

[16] J. S. Manser, J. A. Christians, and P. V. Kamat, Chem. Rev. **116**, 12956 (2016).

[17] J. Even, L. Pedesseau, J.-M. Jancu, and C. K. Katan, J. Phys. Chem. Lett. **4**, 2999 (2013).

[18] E. Mosconi, P. Umari, and F. De Angelis, Phys. Chem. Chem. Phys. **18**, 27158 (2016).

[19] B. A. Gregg, J. Phys. Chem. B **107**, 4688 (2003).

[20] L. M. Herz, Annu. Rev. Phys. Chem. **67**, 65 (2016).

[21] X. Chen, H. Lu, Y. Yang, and M. C. Beard, J. Phys. Chem. Lett. **9**, 2595 (2018).

[22] N. Sestu, M. Cadelano, V. Sarritzu, F. Chen, D. Marongiu, R. Piras, M. Mainas, F. Quochi, M. Saba, A. Mura, and G. Bongiovanni, J. Phys. Chem. Lett. **6**, 4566 (2015).

[23] K. Galkowski, A. Mitioglu, A. Miyata, P. Plochocka, O. Portugall, G. E. Eperon, J. T.-W. Wang, T. Stergiopoulos, S. D. Stranks, H. J. Snaith, and R. J. Nicholas, Energy Environ. Sci. **9**, 962 (2016).

[24] Y. Yang, D. P. Ostrowski, R. M. France, K. Zhu, J. van de Lagemaat, J. M. Luther, and M. C. Beard, Nat. Photonics **10**, 53 (2015).

[25] V. D'Innocenzo, G. Grancini, M. J. P. Alcocer, A. R. S. Kandada, S. D. Stranks, M. M. Lee, G. Lanzani, H. J. Snaith, and A. Petrozza, Nat. Commun. **5**, 3586 (2014).

[26] T. J. Savenije, C. S. Ponseca, L. Kunneman, M. Abdellah, K. Zheng, Y. Tian, Q. Zhu, S. E. Canton, I. G. Scheblykin, T. Pullerits, A. Yartsev, and V. Sundström, J. Phys. Chem. Lett. **5**, 2189 (2014).

[27] Q. Lin, A. Armin, R. C. R. Nagiri, P. L. Burn, and P. Meredith, Nat. Photonics **9**, 106 (2014).

[28] A. Miyata, A. Mitioglu, P. Plochocka, O. Portugall, J. T.-W. Wang, S. D. Stranks, H. J. Snaith, and R. J. Nicholas, Nat. Phys. **11**, 582 (2015).

[29] S. Sun, T. Salim, N. Mathews, M. Duchamp, C. Boothroyd, G. Xing, T. C. Sum, and Y. M. Lam, Energy Environ. Sci. **7**, 399 (2014).

[30] Z. Yang, A. Surrente, K. Galkowski, N. Bruyant, D. K. Maude, A. A. Haghighirad, H. J. Snaith, P. Plochocka, and R. J. Nicholas, J. Phys. Chem. Lett. **8**, 1851 (2017).

[31] S. A. March, C. Clegg, D. B. Riley, D. Webber, I. G. Hill, and K. C. Hall, Sci. Rep. **6**, 39139 (2016).

[32] K. Wu, A. Bera, C. Ma, Y. Du, Y. Yang, L. Li, and T. Wu, Phys. Chem. Chem. Phys. **16**, 22476 (2014).

[33] M. Bokdam, T. Sander, A. Stroppa, S. Picozzi, D. D. Sarma, C. Franchini, and G. Kresse, Sci. Rep. **6**, 28618 (2016).

[34] X. Zhu, H. Su, R. A. Marcus, and M. E. Michel-Beyerle, J. Phys. Chem. Lett. **5**, 3061 (2014).

[35] P. Umari, E. Mosconi, and F. De Angelis, J. Phys. Chem. Lett. **9**, 620 (2018).

[36] T. Ahmed, C. La-o-vorakiat, T. Salim, Y. M. Lam, E. E. M. Chia, and J.-X. Zhu, Europhys. Lett. **108**, 67015 (2014).

[37] J. M. Frost, K. T. Butler, F. Brivio, C. H. Hendon, M. van Schilfgaarde, and A. Walsh, Nano Lett. **14**, 2584 (2014).

[38] J. Even, L. Pedesseau, and C. Katan, J. Phys. Chem. C **118**, 11566 (2014).

[39] E. Menéndez-Proupin, C. L. Beltrán Ríos, and P. Wahnón, Phys. Status Solidi RRL **9**, 559 (2015).

[40] T. Hakamata, K. Shimamura, F. Shimojo, R. K. Kalia, A. Nakano, and P. Vashishta, Sci. Rep. **6**, 19599 (2016).

[41] W.-J. Yin, T. Shi, and Y. Yan, Appl. Phys. Lett. **104**, 063903 (2014).

[42] J. Kim, S.-H. Lee, J. H. Lee, and K.-H. Hong, J. Phys. Chem. Lett. **5**, 1312 (2014).

[43] N. Liu and C. Yam, Phys. Chem. Chem. Phys. **20**, 6800 (2018).

[44] J.-H. Yang, W.-J. Yin, J.-S. Park, and S.-H. Wei, Sci. Rep. **5**, 16977 (2015).

[45] Q. Wang, Y. Shao, H. Xie, L. Lyu, X. Liu, Y. Gao, and J. Huang, Appl. Phys. Lett. **105**, 163508 (2014).

[46] A. Dymshits, A. Henning, G. Segev, Y. Rosenwaks, and L. Etgar, Sci. Rep. **5**, 8704 (2015).

[47] A. Guerrero, E. J. Juarez-Perez, J. Bisquert, I. Mora-Sero, and G. Garcia-Belmonte, Appl. Phys. Lett. **105**, 133902 (2014).

[48] A. Schleife, C. Rödl, F. Fuchs, K. Hannewald, and F. Bechstedt, Phys. Rev. Lett. **107**, 236405 (2011).

[49] A. Kronenberger, A. Polity, D. M. Hofmann, B. K. Meyer, A. Schleife, and F. Bechstedt, Phys. Rev. B **86**, 115334 (2012).

[50] K. Kang, A. Kononov, C.-W. Lee, J. A. Leveillee, E. P. Shapera, X. Zhang, and A. Schleife, Comput. Mater. Sci. **160**, 207 (2019).

[51] G. D. Mahan, Phys. Rev. **153**, 882 (1967).

[52] W. Kohn and L. J. Sham, Phys. Rev. **140**, A1133 (1965).

[53] P. Hohenberg and W. Kohn, Phys. Rev. **136**, B864 (1964).

[54] P. E. Blöchl, Phys. Rev. B **50**, 17953 (1994).

[55] J. P. Perdew, A. Ruzsinszky, G. I. Csonka, O. A. Vydrov, G. E. Scuseria, L. A. Constantin, X. Zhou, and K. Burke, Phys. Rev. Lett. **100**, 136406 (2008).

[56] F. Brivio, J. M. Frost, J. M. Skelton, A. J. Jackson, O. J. Weber, M. T. Weller, A. R. Goñi, A. M. A. Leguy, P. R. F. Barnes, and A. Walsh, Phys. Rev. B **92**, 144308 (2015).

[57] P. S. Whitfield, N. Herron, W. E. Guise, K. Page, Y. Q. Cheng, I. Milas, and M. K. Crawford, Sci. Rep. **6**, 35685 (2016).

[58] K. T. Butler, J. M. Frost, and A. Walsh, Mater. Horiz. **2**, 228 (2015).

[59] F. F. Targhi, Y. S. Jalili, and F. Kanjouri, Results Phys. **10**, 616 (2018).

[60] M. Gajdoš, K. Hummer, G. Kresse, J. Furthmüller, and F. Bechstedt, Phys. Rev. B **73**, 045112 (2006).

[61] J. P. Perdew, K. Burke, and M. Ernzerhof, Phys. Rev. Lett. **77**, 3865 (1996).

[62] P. Umari, E. Mosconi, and F. Angelis, Sci. Rep. **4**, 4467 (2014).

[63] S. Steiner, S. Khmelevskyi, M. Marsmann, and G. Kresse, Phys. Rev. B **93**, 224425 (2016).

[64] M. Rohlfing and S. G. Louie, Phys. Rev. B **62**, 4927 (2000).

[65] F. Fuchs, C. Rödl, A. Schleife, and F. Bechstedt, Phys. Rev. B **78**, 085103 (2008).

[66] F. Bechstedt, R. D. Sole, G. Cappellini, and L. Reining, Solid State Commun. **84**, 765 (1992).

[67] G. Cappellini, R. Del Sole, L. Reining, and F. Bechstedt, Phys. Rev. B **47**, 9892 (1993).

[68] A. Schleife, *Electronic and Optical Properties of MgO, ZnO, and CdO* (Südwestdeutscher Verlag für Hochschulschriften, Saarbrücken, Germany, 2011).

[69] A. Schleife, Exciting imperfection: Real-structure effects in magnesium-, cadmium-, and zinc-oxide, Ph.D. thesis, Friedrich-Schiller-Universität, Jena, 2010.

[70] K. F. Berggren and B. E. Sernelius, Phys. Rev. B **24**, 1971 (1981).

[71] See Supplemental Material at http://link.aps.org/supplemental/10.1103/PhysRevB.100.035205 for additional and auxiliary content of this paper.

[72] H. Peelaers, E. Kioupakis, and C. G. Van de Walle, Phys. Rev. B **92**, 235201 (2015).

[73] G. Kresse and D. Joubert, Phys. Rev. B **59**, 1758 (1999).

[74] G. Kresse and J. Furthmüller, Phys. Rev. B **54**, 11169 (1996).

[75] M. Shishkin and G. Kresse, Phys. Rev. B **74**, 035101 (2006).

[76] C. Rödl, F. Fuchs, J. Furthmüller, and F. Bechstedt, Phys. Rev. B **77**, 184408 (2008).

[77] J. Leveillee and A. Schleife (2019), doi:10.18126/M2D64J; B. Blaiszik, K. Chard, J. Pruyne, R. Ananthakrishnan, S. Tuecke, and I Foster, JOM **68**, 2045 (2016).

[78] K. P. Ong, T. W. Goh, Q. Xu, and A. Huan, J. Phys. Chem. A **119**, 11033 (2015).

[79] W. Kong, Z. Ye, Z. Qi, B. Zhang, M. Wang, A. Rahimi-Iman, and H. Wu, Phys. Chem. Chem. Phys. **17**, 16405 (2015).

[80] M. R. Filip and F. Giustino, Phys. Rev. B **90**, 245145 (2014).

[81] A. S. Thind, X. Huang, J. Sun, and R. Mishra, Chem. Mater. **29**, 6003 (2017).

[82] C. Quarti, E. Mosconi, J. M. Ball, V. D'Innocenzo, C. Tao, S. Pathak, H. J. Snaith, A. Petrozza, and F. De Angelis, Energy Environ. Sci. **9**, 155 (2016).

[83] M. R. Filip, C. Verdi, and F. Giustino, J. Phys. Chem. C **119**, 25209 (2015).

[84] F. Brivio, K. T. Butler, A. Walsh, and M. van Schilfgaarde, Phys. Rev. B **89**, 155204 (2014).

[85] M. A. Pérez-Osorio, R. L. Milot, M. R. Filip, J. B. Patel, L. M. Herz, M. B. Johnston, and F. Giustino, J. Phys. Chem. C **119**, 25703 (2015).

[86] M. Sendner, P. K. Nayak, D. A. Egger, S. Beck, C. Muller, B. Epding, W. Kowalsky, L. Kronik, H. J. Snaith, A. Pucci, and R. Lovrincic, Mater. Horiz. **3**, 613 (2016).

[87] A. Poglitsch and D. Weber, J. Chem. Phys. **87**, 6373 (1987).

[88] J. Feng and B. Xiao, J. Phys. Chem. Lett. **5**, 1278 (2014).

[89] G. Giorgi, J.-I. Fujisawa, H. Seqawa, and K. Yamashita, J. Phys. Chem. Lett. **4**, 4213 (2013).

[90] L. Pedesseau, D. Sapori, B. Traore, R. Robles, H.-H. Fang, M. A. Loi, H. Tsai, W. Nie, J.-C. Blancon, A. Neukirch, S. Tretiak, A. D. Mohite, C. Katan, J. Even, and M. Kepenekian, ACS Nano **10**, 9776 (2016).

[91] N.-G. Park, Mater. Today **18**, 65 (2015).

[92] T. Etienne, E. Mosconi, and F. De Angelis, J. Phys. Chem. Lett. **7**, 1638 (2016).

[93] E. Mosconi, T. Etienne, and F. De Angelis, J. Phys. Chem. Lett. **8**, 2247 (2017).

[94] J. S. Manser and P. V. Kamat, Nat. Photonics **8**, 737 (2014).

[95] M. Shirayama, H. Kadowaki, T. Miyadera, T. Sugita, M. Tamakoshi, M. Kato, T. Fujiseki, D. Murata, S. Hara, T. N. Murakami, S. Fujimoto, M. Chikamatsu, and H. Fujiwara, Phys. Rev. Appl. **5**, 014012 (2016).

[96] C.-W. Chen, S.-Y. Hsiao, C.-Y. Chen, H.-W. Kang, Z.-Y. Huang, and H.-W. Lin, J. Mater. Chem. A **3**, 9152 (2015).

[97] P. Löper, M. Stuckelberger, B. Niesen, J. Werner, M. Filipič, S.-J. Moon, J.-H. Yum, M. Topič, S. D. Wolf, and C. Ballif, J. Phys. Chem. Lett. **6**, 66 (2015).

[98] F. Bechstedt, K. Seino, P. H. Hahn, and W. G. Schmidt, Phys. Rev. B **72**, 245114 (2005).

[99] J. Fu, Q. Xu, G. Han, B. Wu, C. H. A. Huan, M. L. Leek, and T. C. Sum, Nat. Commun. **8**, 1300 (2017).

[100] D. A. Valverde-Chávez, C. S. Ponseca, C. C. Stoumpos, A. Yartsev, M. G. Kanatzidis, V. Sundström, and D. G. Cooke, Energy Environ. Sci. **8**, 3700 (2015).

[101] D. Shi, V. Adinolfi, R. Comin, M. Yuan, E. Alarousu, A. Buin, Y. Chen, S. Hoogland, A. Rothenberger, K. Katsiev, Y. Losovyj, X. Zhang, P. A. Dowben, O. F. Mohammed, E. H. Sargent, and O. M. Bakr, Science **347**, 519 (2015).